IEEE Access
Multidisciplinary | Rapid Review | Open Access Journal

Received 19 September 2022, accepted 9 October 2022, date of publication 19 October 2022, date of current version 28 October 2022.

Digital Object Identifier 10.1109/ACCESS.2022.3215720

RESEARCH ARTICLE

Equilibrium Configuration Analysis and Equilibrium-Based Trajectory Generation Method for Under-Constrained Cable-Driven Parallel Robot

SUNG WOOK HWANG, DEOK HA KIM, JAEHWAN PARK, AND JONG HYEON PARK, (Member, IEEE)
Department of Mechanical Engineering, Hanyang University, Seoul 04763, South Korea

Corresponding author: Jong Hyeon Park (jongpark@hanyang.ac.kr)

This work was supported by the National Research Foundation of Korea and funded by the Ministry of Science and ICT (Information and Communication Technology) under Grant No. 2021R1A2C1012614.

ABSTRACT Under-constrained cable-driven parallel robots (UCCDPRs) manipulate the end-effector (EE) by employing fewer number of cables than the degree of freedom of the EE, which causes unwanted swaying motions and oscillations. These unwanted vibrations can be suppressed by using the regenerated EE trajectory through the input-shaper. However, in the case of the UCCDPR systems, generating the feasible EE trajectory and deriving the natural frequency for designing the input-shaper is not straightforward since finding the stable equilibrium configuration is challenging. This paper proposes a novel methodology to find the stable equilibrium configuration of the general UCCDPRs in the assigned EE position. With the proposed method, the EE trajectory can be reproduced as a vibration suppression trajectory through an input shaper designed based on the analysis of the natural frequencies, as well as generating feasible EE trajectories based on the equilibrium configuration. Also, even if the orientation trajectory is not given and only the position trajectory is given, the cable length to follow the given position trajectory of the EE can be obtained based on the equilibrium configuration corresponding to the given position trajectory. Computer simulations and hardware experiments were conducted to verify the effectiveness and performance of the proposed method.

INDEX TERMS Cable-driven parallel robots, underconstrained robots, underactuated robots, equilibrium configuration, natural frequency, input shaping, trajectory generation.

I. INTRODUCTION

Cable-driven parallel robots (CDPRs) are a group of parallel robots that control their end-effector (EE) or payload by employing several cables, instead of rigid links, actuated by servo-controlled winches. CDPRs have many advantages compared with conventional link-based parallel and serial manipulators. Since cables have low inertia, the mass of the total moving parts of a CDPR system is small, making high-speed operations possible and reducing its energy consumption. In addition, CDPRs can have a broad workspace and their structural simplicity makes it easy to adjust the size of their workspace and assemble and disassemble them. These features make CDPR systems employed in various application fields despite some disadvantages caused by cable properties such as flexibility, sagging, and unidirectional force transmission. Among different types of CDPRs, under-constrained CDPRs (UCCDPRs), which use fewer number of cables than the degrees of freedom (DoFs) of their EE, have been frequently used in applications such as measurement, rescue, service, and construction fields due to the simplicity of their structure, low cost, expandability of workspace, etc., [1], [2], [3], [4], [5], [6], [7], [8], [9].

However, an UCCDPR has a fundamental drawback brought about by structural distinction. Since the number of cables used is fewer than the DoFs of the EE, some DoFs

The associate editor coordinating the review of this manuscript and approving it for publication was Hassen Ouakad.

are constrained by the cables but not the others. Even with the control of the cables and the gravity pull of the EE, the generalized coordinates of the EE are not uniquely determined, causing unwanted oscillatory motions of the EE. This property unique to UCCDPRs raises a few challenging problems such as finding a stable equilibrium configuration [10], finding a feasible solution set of the forward and inverse kinematics [11], [12], [13], [14], [15], [16], [17], [18], and subduing unwanted oscillatory motions of the EE [19], [20], [21], [22], [23], [24], [25], [26], [27], [28], [29], [30], [31], [32], [33], [34], [35], [36].

One research group conducted a stability analysis of UCCDPR static equilibrium by applying a constrained optimization based on ordinary linear-algebra routines [10]. Moreover, they proposed methodologies to solve the forward kinematics for general UCCDPRs when each cable length is assigned based on kinematic constraints and mechanical equilibrium equations [11], [12], [13], [14]. A general method for solving the forward kinematic problem was represented in [12], which sets the problem by a set of algebraic equations, finding a least-degree univariate polynomial based on homotopy-continuation algorithms. In [14], feasible solutions satisfying the positive cable tensions were directly found by using interval analysis. Another research group proposed an unsupervised neural network algorithm to conduct real-time forward kinematic analysis by modeling the problem as determining a nonlinear function approximation [15], [16].

While intensive research has been conducted on the forward kinematics of UCCDPRs, relatively few research works were done on their inverse kinematics. The length of each cable for a given EE pose can be straightforwardly calculated through the kinematic constraints of the UCCDPR, but if the EE pose assigned to solve the inverse kinematics is not a feasible pose reflecting the characteristics of the UCCDPR, then the pose cannot be realized by the cable length obtained through the inverse kinematics. Finding the feasible cable length at an assigned EE position was researched on a 2-cable UCCDPR in the 2-dimensional plane and 3-cable UCCDPR in the 3-dimensional space [34], [36]. In [17] and [18], studies were conducted to find a solution set of the inverse kinematics for two cases where EE's position or orientation is given for 3- and 4-cable UCCDPR systems. However, the methods proposed in the above-introduced research have limitations in their application to apply to all types of UCCDPR since they can only work under special cases where the UCCDPR is constructed with 2 and 3 cables or special constraints on the EE are used.

Since the EE of UCCDPRs is not fully constrained, unwanted oscillatory motions may occur. Moreover, if the proper EE trajectory reflecting the features of the underconstrained system is not used, such motions can get worse. To suppress and prevent these unwanted motions of the EE, much research on pre-planning a trajectory for UCCDPRs has been carried out. A method to plan a trajectory based on the inverse dynamics and antisway control method was proposed in [19] and [20]. And a trajectory tracking method on the basis of flatness control was researched in [21]. Other research groups proposed a trajectory planning method to extend the workspace beyond the static equilibrium workspace by using natural frequencies of UCCDPR caused by the preserved DoFs of the EE [22], [23], [24], [25], [26], [27], [28], [29]. And a rest-to-rest trajectory planning method was proposed by finding the solutions of the equations of motion of the UCCDPR satisfying given boundary value and constraints on position and velocity at start and end times [30]. Also, trajectory generation methods to suppress unwanted oscillations of EE were proposed by using an input shaping algorithm based on the analysis of natural frequencies [31], [32], [33], [34], [35], [36]. However, all the above-mentioned studies were conducted only on 2- and 3-cable UCCDPR, Gentry, Crane types, or generating simple linear trajectories for 4-cable systems.

This paper proposes a methodology to find an equilibrium configuration for a given EE position in the workspace of generic m-cable UCCDPRs. Through the proposed method, it is possible to generate a feasible EE trajectory for various paths based on the equilibrium configuration and to calculate the cable lengths that make the EE follow a given position trajectory. In addition, the proposed method allows a frequency analysis at all positions in the workspace by linearizing the dynamics of the UCCDPR around an equilibrium point obtained from the proposed method. Thus, it is possible to apply an input shaping algorithm to generic UCCDPRs to suppress the unwanted oscillatory motion of the EE. The key research contributions presented in this paper are summarized as follows.

1) A novel methodology to find the equilibrium configuration of the generic UCCDPRs with m cables ($1<m<6$) is proposed.
2) An equilibrium-based trajectory (EQBT) of the EE can be generated through the proposed method, which makes it possible to obtain a feasible cable length that allows the EE to track a given position trajectory even if the orientation is not given in the UCCDPR used 4 cables or more.
3) This paper also shows how the proposed method can be used to derive linearized internal dynamics expressed by free variables only, which in turn yields the information on frequencies, which are used in input shaping algorithms.

This paper is organized as follows. In Section II, the analysis on the kinematics of the UCCDPRs is described. Section III investigates the dynamic of the UCCDPRs and their internal dynamics. In Section IV, the proposed method to find the equilibrium configuration of the UCCDPRs is explained and the analysis on the natural frequencies is conducted. In Section V, the zero-vibration (ZV) and zero-vibration and derivative (ZVD) input shaper based on the natural frequencies is applied in order to generate the oscillation suppression trajectory. Section VI shows the validation and

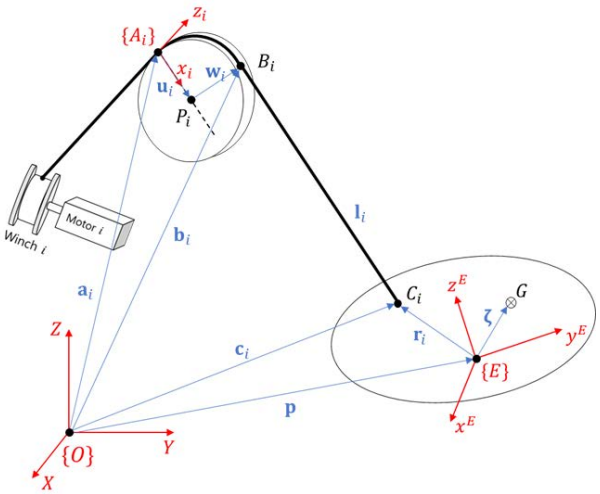

FIGURE 1. Schematic configuration of UCCDPR on the ith cable.

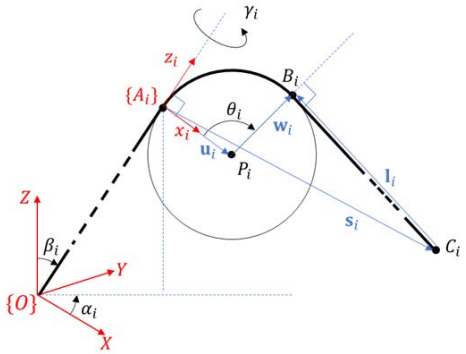

FIGURE 2. Pulley diagram on the pulley plane (x_i-z_i plane).

effectiveness of the proposed method through the simulations and experiments, followed by the conclusions of this work in Section VII.

II. KINEMATIC ANALYSIS

A. KINEMATICS

The schematic diagram shown in Fig. 1 shows the structure of a generic m-cable UCCDPR, where $1 < m < 6$, with more focus on cable i. The inertial coordinate frame $\{O\}$ is attached to the ground, which is one of the vertical posts in this paper, and a moving coordinate frame $\{E\}$ is attached to an arbitrary point, point E, on the EE. The generalized coordinate configuration related to an EE pose is defined as $\mathbf{q} = [\mathbf{p}^T \ \boldsymbol{\eta}^T]^T \in \mathbb{R}^n$, where $\mathbf{p} = [x \ y \ z]^T$ represents the position vector of the origin of $\{E\}$, and $\boldsymbol{\eta} = [\phi \ \theta \ \psi]^T$ is the Euler-angle vector based on Z-Y-X for the orientation of $\{E\}$ with respect to $\{O\}$. Let $\mathbf{R}$ denote the rotation matrix describing the orientation of the EE with respect to the coordinate frame $\{O\}$. Thus,

$$\mathbf{R} \triangleq \mathbf{R}_z(\psi)\mathbf{R}_y(\theta)\mathbf{R}_x(\phi) \tag{1}$$

where $\mathbf{R}_z$, $\mathbf{R}_y$, and $\mathbf{R}_x$ denote rotation matrices about Z-, Y-, and X-axes, respectively. And point G is the center of mass (COM) of the EE, and $\boldsymbol{\zeta}$ is the related position of the COM with respect to position point E.

Coordinate frame $\{A_i\}$ is attached to pulley i at its groove, denoted by A_i, such that its z_i-axis is always tangential to pulley i and aligned with the cable coming from the winch driven by motor i. As shown in Fig. 2, let α_i and β_i angles be invariant and known once the UCCDPR is installed. The x_i-axis of $\{A_i\}$ heads toward point P_i, the center of the pulley. Let the x_i-z_i plane of $\{A_i\}$ be called the pulley plane in this paper. The pulley plane rotates passively depending on the EE pose along the z_i-axis, and γ_i denotes its swivel angle. Thus, the orientation of $\{A_i\}$ can be expressed by

$$\mathbf{R}_i \triangleq \mathbf{R}_i^*(\alpha_i, \beta_i)\mathbf{R}_{z_i}(\gamma_i). \tag{2}$$

Note that rotation matrix $\mathbf{R}_i^*$ is constant. Also note that point B_i is the point at which cable i comes out of the pulley, and $\mathbf{u}_i$ and $\mathbf{w}_i$ are the position vectors from point A_i to point P_i and from point P_i to point B_i, respectively, and a wrap angle, θ_i, denotes the obtuse angle between $\mathbf{u}_i$ and $\mathbf{w}_i$. Vector $\mathbf{r}_i$ denotes the vector from the origin of $\{E\}$ to point C_i, where cable i is attached to the EE. In Figs. 1 and 2, it is clear that

$$\mathbf{l}_i = \mathbf{u}_i + \mathbf{w}_i - \mathbf{s}_i \tag{3}$$

where

$$\mathbf{s}_i \triangleq \mathbf{c}_i - \mathbf{a}_i \tag{4}$$

$$\mathbf{c}_i = \mathbf{p} + \mathbf{r}_i \tag{5}$$

Note that since vector $\mathbf{a}_i$ is invarient, vector $\mathbf{s}_i$ depends on vector $\mathbf{c}_i$. The length of cable i from point C_i to point B_i, which is equal to the norm of $\mathbf{l}_i$, i.e, $\ell_i = \|\mathbf{l}_i\|$, can be expressed as

$$\ell_i = L_i - r_i\theta_i \tag{6}$$

where L_i is the length of cable i from point C_i to point A_i, and r_i are the radius of pulley i. See Appendix VII for the details on Eq. (6).

Thus, the kinematic constraints expressed as vector form in Eq. (3) can be rewritten by considering only its magnitude:

$$\mathbf{0} = \boldsymbol{\Phi}(\mathbf{q}, \boldsymbol{\ell}) \in \mathbb{R}^m \tag{7}$$

where the ith element of $\boldsymbol{\Phi}$ is $\phi_i = \ell_i^2 - \mathbf{l}_i^T\mathbf{l}_i$, and $\boldsymbol{\ell} = [\ell_1 \ \ell_2 \ \cdots \ \ell_m]^T$.

B. DIFFERENTIAL KINEMATICS

Let $\boldsymbol{\omega}$ denote the angular velocity of the EE. Then,

$$\boldsymbol{\omega} = \mathbf{W}(\boldsymbol{\eta})\dot{\boldsymbol{\eta}} \tag{8}$$

where

$$\mathbf{W}(\boldsymbol{\eta}) \triangleq \begin{bmatrix} \cos\psi\cos\theta & -\sin\psi & 0 \\ \sin\psi\cos\theta & \cos\psi & 0 \\ -\sin\theta & 0 & 1 \end{bmatrix}. \tag{9}$$

The velocity of point G is

$$\mathbf{v}_G = \dot{\mathbf{p}} + \boldsymbol{\omega} \times \boldsymbol{\zeta}. \tag{10}$$

And the velocity of point C_i is

$$\dot{\mathbf{c}}_i = \dot{\mathbf{p}} + \boldsymbol{\omega} \times \boldsymbol{r}_i. \tag{11}$$

The rate of changes in cable length, $\mathbf{L} = [L_1 \cdots L_m]^T$, and EE pose, $\mathbf{q}$, can be described by differentiating the kinematic constraints, Eq. (7) (The details are explained in Appendix VII.):

$$\dot{\mathbf{L}} = -\mathbf{J}\mathbf{D}\dot{\mathbf{q}} = -\mathbf{J}_d\dot{\mathbf{q}} \tag{12}$$

where

$$\mathbf{J} = \begin{bmatrix} \vdots & \vdots \\ \hat{\mathbf{l}}_i^T & (\mathbf{r}_i \times \hat{\mathbf{l}}_i)^T \\ \vdots & \vdots \end{bmatrix} \in \mathbb{R}^{m\times n} \tag{13}$$

$$\mathbf{D} = \begin{bmatrix} \mathbf{I}_3 & \mathbf{0}_{3\times 3} \\ \mathbf{0}_{3\times 3} & \mathbf{W}(\boldsymbol{\eta}) \end{bmatrix} \in \mathbb{R}^{n\times n}, \tag{14}$$

and $\mathbf{I}_3$ and $\mathbf{0}_{3\times 3}$ represent the 3×3 identity matrix and zero matrix, respectively. $\hat{\mathbf{l}}_i$ denotes the unit vector of $\mathbf{l}_i$, i.e., $\hat{\mathbf{l}}_i = \mathbf{l}_i/\ell_i$, $\mathbf{J}$ and $\mathbf{J}_d$ are called the kinematic and the analytic Jacobian, respectively, and they have the same rank because columns of $\mathbf{W}$ are mutually independent except for the case when the EE stays at the edge of the workspace, i.e., $\phi = \pm\pi/2$ or $\theta = \pm\pi/2$ or $\psi = \pm\pi/2$. In the case of the UCCDPR system, the rank r is less than or equal to m, i.e., $\text{rank}(\mathbf{J}) = \text{rank}(\mathbf{J}_d) = r \leq m$, the number of free variables among $\dot{\mathbf{q}}$ is $p = n - r$. Thus, nullspace of Jacobian is expressed by

$$\dot{\mathbf{q}}_{null} = \mathbf{J}_d^*\boldsymbol{\nu} \in N(\mathbf{J}_d) \quad \text{for any } \boldsymbol{\nu} \in \mathbb{R}^p \tag{15}$$

where columns of $\mathbf{J}_d^* \in \mathbb{R}^{n\times p}$ span the nullspace of $\mathbf{J}_d$ and $\dot{\mathbf{q}}_{null} \subset \mathbb{R}^n$. Thus, Eq. (12) can be rewritten as

$$\dot{\mathbf{L}} = -\mathbf{J}_d\left(\dot{\mathbf{q}} + \dot{\mathbf{q}}_{null}\right) \tag{16}$$

with

$$\mathbf{J}_d\dot{\mathbf{q}}_{null} = \mathbf{0} \tag{17}$$

It means that the EE can still move with $\dot{\mathbf{q}}_{null} \neq \mathbf{0}$ even if $\dot{\mathbf{L}} = \ddot{\mathbf{L}} = \mathbf{0}$, with all the cables taut.

Generally, $\text{rank}(\mathbf{J}_d) = m$. However, a kinematic singularity may arise, i.e., $\text{rank}(\mathbf{J}_d) < m$. In this case, the singularity can be avoided by adjusting the cable connecting points, C_i for cable i. Thus, it is assumed in this paper that $\text{rank}(\mathbf{J}_d) = m$.

III. MOTION ANALYSIS

A. DYNAMICS

In this section, the equations of motion (EOMs) are derived based on the Euler-Lagrange method to analyze the behaviors of the EE. The kinetic energy of the EE is

$$K = \frac{1}{2}m\mathbf{v}_G^T\mathbf{v}_G + \frac{1}{2}\boldsymbol{\omega}^T\mathbf{I}_G\boldsymbol{\omega} \tag{18}$$

where m and $\mathbf{I}_G$ denote the mass and the moment of inertia of the EE, respectively. And the potential energy of the EE is

$$P = mg\hat{\mathbf{k}}^T(\mathbf{p} + \boldsymbol{\zeta}) \tag{19}$$

where g denotes the acceleration of gravity.

The Lagrangian is defined as

$$\mathcal{L} \triangleq K - V, \tag{20}$$

and the extended Lagrangian is defined with Lagrange multiplier $\boldsymbol{\lambda}$ to reflect the holonomic constraints:

$$\mathcal{L}_e \triangleq \mathcal{L} + \sum_{i=1}^{m}\phi_i\lambda_i = \mathcal{L} + \boldsymbol{\Phi}^T\boldsymbol{\lambda} \tag{21}$$

where λ_i denotes the ith component of $\boldsymbol{\lambda} \in \mathbb{R}^m$, which represents the constraint forces, that is, the cable tensions applied at the EE.

Then, the EOM becomes

$$\frac{d}{dt}\left(\frac{\partial\mathcal{L}_e}{\partial\dot{\mathbf{q}}}\right) - \frac{\partial\mathcal{L}_e}{\partial\mathbf{q}} = \mathbf{0} \tag{22a}$$

or

$$\frac{d}{dt}\left(\frac{\partial\mathcal{L}}{\partial\dot{\mathbf{q}}}\right) - \frac{\partial\mathcal{L}}{\partial\mathbf{q}} = \Xi^T\boldsymbol{\lambda} \tag{22b}$$

where

$$\Xi = \frac{\partial\boldsymbol{\Phi}}{\partial\mathbf{q}} \in \mathbb{R}^{m\times n}. \tag{23}$$

Note that $\Xi^T\boldsymbol{\lambda}$ is the generalized force applied at the EE caused by the cable tensions. Thus, the nonlinear dynamics of the UCCDPR in Eq. (22a) or Eq. (22b) can be organized by EE state variables and cable tensions:

$$\mathbf{M}(\mathbf{q})\ddot{\mathbf{q}} + \mathbf{C}(\mathbf{q}, \dot{\mathbf{q}})\dot{\mathbf{q}} + \mathbf{G}(\mathbf{q}) = \mathbf{J}_d^T\mathbf{T} \tag{24}$$

where

$$\mathbf{M}(\mathbf{q}) = \begin{bmatrix} m\mathbf{I}_3 & -m[\boldsymbol{\zeta}]_\times\mathbf{W}(\boldsymbol{\eta}) \\ m\mathbf{W}^T(\boldsymbol{\eta})[\boldsymbol{\zeta}]_\times & \mathbf{W}^T(\boldsymbol{\eta})\mathbf{I}_E\mathbf{W}(\boldsymbol{\eta}) \end{bmatrix} \in \mathbb{R}^{n\times n} \tag{25}$$

$$\mathbf{C}(\mathbf{q}, \dot{\mathbf{q}}) = \begin{bmatrix} \mathbf{0}_{3\times 3} & -m\left([\boldsymbol{\zeta}]_\times\dot{\mathbf{W}}(\boldsymbol{\eta}) + [\boldsymbol{\omega}]_\times[\boldsymbol{\zeta}]_\times\mathbf{W}(\boldsymbol{\eta})\right) \\ \mathbf{0}_{3\times 3} & \mathbf{W}^T(\boldsymbol{\eta})\left(\mathbf{I}_E\dot{\mathbf{W}}(\boldsymbol{\eta}) + [\boldsymbol{\omega}]_\times\mathbf{I}_E\mathbf{W}(\boldsymbol{\eta})\right) \end{bmatrix} \in \mathbb{R}^{n\times n} \tag{26}$$

$$\mathbf{G}(\mathbf{q}) = mg\begin{bmatrix} \mathbf{i}_z \\ \mathbf{W}^T(\boldsymbol{\eta})[\boldsymbol{\zeta}]_\times\mathbf{i}_z \end{bmatrix} \in \mathbb{R}^n \tag{27}$$

$$\mathbf{T} = \begin{bmatrix} \cdots & T_i & \cdots \end{bmatrix}^T \in \mathbb{R}^m \tag{28}$$

$$\mathbf{I}_E = \mathbf{I}_G + m[\boldsymbol{\zeta}]_\times^T[\boldsymbol{\zeta}_\times]. \tag{29}$$

Note that symbol $[\cdot]_\times$ denotes a 3×3 skew-symmetric matrix to represent cross product of vectors as a matrix multiplication, i.e., $\mathbf{u} \times \mathbf{v} \triangleq [\mathbf{u}]_\times\mathbf{v}$ for $\mathbf{u}, \mathbf{v} \in \mathbb{R}^3$, and T_i denotes the tension in cable i.

B. INTERNAL DYNAMICS

By pre-multiplying a permutation matrix $\mathbf{P} \in \mathbb{R}^{n\times n}$ by $\mathbf{q}$, $\mathbf{q}$ can be separated into constrained state variables $\mathbf{q}_c \in \mathbb{R}^m$ related to constrained DoFs of the EE, and free state variables $\mathbf{q}_f \in \mathbb{R}^p$ related to free DoFs of the EE.

$$\mathbf{q}_p \triangleq \mathbf{P}\mathbf{q} = \begin{bmatrix} \mathbf{q}_c^T & \mathbf{q}_f^T \end{bmatrix}^T. \tag{30}$$

And the UCCDPR's EOM can be split into two equations by pre-multiplying $\mathbf{P}$ by both sides of Eq. (22):

$$\frac{d}{dt}\left(\frac{\partial \mathcal{L}}{\partial \dot{\mathbf{q}}_c}\right) - \frac{\partial \mathcal{L}}{\partial \mathbf{q}_c} = \Xi_c^T \boldsymbol{\lambda} \in \mathbb{R}^m \tag{31a}$$

$$\frac{d}{dt}\left(\frac{\partial \mathcal{L}}{\partial \dot{\mathbf{q}}_f}\right) - \frac{\partial \mathcal{L}}{\partial \mathbf{q}_f} = \Xi_f^T \boldsymbol{\lambda} \in \mathbb{R}^p \tag{31b}$$

where $\Xi_c = \partial \boldsymbol{\Phi}/\partial \mathbf{q}_c \in \mathbb{R}^{m\times m}$ and $\Xi_f = \partial \boldsymbol{\Phi}/\partial \mathbf{q}_f \in \mathbb{R}^{m\times p}$.

By substituting Eq. (31a) in Eq. (31b) to remove $\boldsymbol{\lambda}$, the *internal dynamics* of the UCCDPR can be obtained as follows.

$$\begin{aligned}\mathbf{0} &= \frac{d}{dt}\left(\frac{\partial \mathcal{L}}{\partial \dot{\mathbf{q}}_f}\right) - \frac{\partial \mathcal{L}}{\partial \mathbf{q}_f} - \Xi_f^T \Xi_c^{-T}\left(\frac{d}{dt}\left(\frac{\partial \mathcal{L}}{\partial \dot{\mathbf{q}}_c}\right) - \frac{\partial \mathcal{L}}{\partial \mathbf{q}_c}\right) \\ &\triangleq \boldsymbol{\mathcal{D}}\left(\mathbf{q}, \dot{\mathbf{q}}, \ddot{\mathbf{q}}\right) \in \mathbb{R}^p\end{aligned} \tag{32}$$

Note that Eq. (32) is a function of both free and constrained state variables, and it can describe the free motion in free state variables in accordance with the motion of constrained state variables.

IV. ANALYSIS OF EQUILIBRIUM CONFIGURATION AND NATRUAL FREQUENCY

A. METHODOLOGY TO FIND EQUILIBRIUM CONFIGURATIONS

Finding a stable equilibrium configuration of the UCCDPR is necessary to find the feasible solution of the inverse kinematics and to analyze the natural frequency to be covered later. In this section, a novel method is proposed to find all equilibrium configurations of the UCCDPR, the cable lengths and the cable tensions as well as the orientation of the EE, when the position of the EE is assigned. The equilibrium configuration can be analyzed by finding the solution satisfying the statics and the kinematic constraints in Eq. (7), simultaneously. The statics of the UCCDPR system can be described by setting $\dot{\mathbf{q}} = \ddot{\mathbf{q}} = \mathbf{0}$ in Eq. (24) as follows.

$$\mathbf{G}(\mathbf{q}) - \mathbf{J}_d^T \mathbf{T} = \mathbf{0}. \tag{33}$$

Note that the statics and kinematic constraints consist of $n + m$ nonlinear equations: n equations in Eq. (33) and m kinematic constraint equations in Eq. (7). Note also that there are $n + 2m$ variables: $\mathbf{q}$, $\mathbf{L}$, and $\mathbf{T}$. Therefore, state variables that define the behavior for the UCCDPR in the steady-state are $\mathbf{X} \triangleq \left[\mathbf{q}_0^T, \mathbf{L}_0^T, \mathbf{T}_0^T\right]^T$, and if the position $\mathbf{p}_0$ of the EE is assigned, unknown state variables of these equations become $\mathbf{X}_u \triangleq \left[\boldsymbol{\eta}_0^T, \mathbf{L}_0^T, \mathbf{T}_0^T\right]^T$. Here, a symbol with subscript '0' denotes a variable at static equilibrium.

In the cases of a 2-cable system in a 2-dimensional plane and a 3-cable system in a 3-dimensional space, if $\mathbf{p}_0$ is given, the number of equations in Eqs. (7) and (33) is equal to the number of unknown variables in them; therefore, these cases are determined systems. Thus, all unknowns can be uniquely determined by considering the constraint conditions related to feasible solution ranges [34], [36]. However, 4- and 5-cable systems in 3-dimensional space are underdetermined because the number of equations is less than the number of unknowns, thus there exist infinitely many solution sets even though the same constraint conditions used in previous research are given.

To find the unique feasible solution satisfying Eqs. (7) and (33), a numerical procedure based on the convex analysis and optimization with constraints for feasibility is applied. The optimization problem is defined by designing the objective function as the 2-norm of statics and by considering the constraints that all cables are taut and that no twisting or interference occurs at the cables as follows:

$$\min_{\mathbf{X}_u} \|\mathbf{G}(\mathbf{q}) - \mathbf{J}_d^T \mathbf{T}\|^2 \tag{34}$$

subject to

$$\text{Equality constraints:} \quad \phi_i\left(\ell_i, \mathbf{q}\right) = 0, \quad \forall i \tag{35a}$$

$$\text{Inequality conditions:} \quad 0 < T_i, \quad \forall i \tag{35b}$$

$$|\phi|, |\theta|, |\psi| < \pi/2. \tag{35c}$$

Note that the objective function, Eq. (34), has a minimum point at zero and the kinematic constraints are reflected as the equality constraints, Eq. (35a). The cable sagging can be prevented by the minimum tension constraints expressed in Eq. (35b) and the twisting and interference of each cable can be avoided by the bounded range of the orientation of the EE expressed in Eq. (35c).

The optimal solution can be found through an interior-point algorithm. By confirming that all eigenvalues of the Hessian matrix, $\mathbf{H}$, expressed by Eq. (36) are larger than 0, it is possible to confirm that the solution is the minimum point within a given constraint.

$$\mathbf{H} = \nabla^2 f + \sum_i \lambda_i \nabla^2 \phi_i \tag{36}$$

Through the proposed method, it is possible to construct a map of $\mathbf{X}_u$ in a given $\mathbf{p}_0$, and it can be used to generate a trajectory based on the equilibrium, called equilibrium-based trajectory (EQBT) in this paper, even when given only the EE position trajectory.

B. ANALYSIS OF NATURAL FREQUENCY

To regenerate the trajectory to suppress the unwanted oscillatory motions through the input-shaper, the analysis of the natural frequency of the UCCDPR should be carried out and the quantity of the natural frequency at the position where the EE is located should be also found. In the case of the general m-cable UCCDPR, the number of normal modes is equal to the dimension of Eq. (32).

To find the natural frequency of the UCCDPR system, the nonlinear internal dynamics, Eq. (32), should be linearized around equilibrium points based on the perturbation method. When oscillations of the EE arise at an equilibrium configuration of the EE, the constrained and free state variables can be expressed as

$$\mathbf{q}_c = \mathbf{q}_{c,0} + \delta \mathbf{q}_c \tag{37}$$

$$\mathbf{q}_f = \mathbf{q}_{f,0} + \delta \mathbf{q}_f \tag{38}$$

where $\delta\mathbf{q}_c$ and $\delta\mathbf{q}_f$ denote perturbations bounded in a small range when the EE sways at the equilibrium configuration. Thus, by applying the fact that it can be possible to neglect the effect of the quadratic and higher-order terms of perturbation variables, the linearized internal dynamics can be represented as follows:

$$\begin{aligned}\mathcal{D}_0\left(\mathbf{q},\dot{\mathbf{q}},\ddot{\mathbf{q}}\right) = \mathcal{D}\left(\mathbf{q}_0,\dot{\mathbf{q}}_0,\ddot{\mathbf{q}}_0\right) + \mathbf{M}_c\delta\ddot{\mathbf{q}}_c \\ +\mathbf{M}_f\delta\ddot{\mathbf{q}}_f + \mathbf{C}_c\delta\dot{\mathbf{q}}_c + \mathbf{C}_f\delta\dot{\mathbf{q}}_f \\ +\mathbf{K}_c\delta\mathbf{q}_c + \mathbf{K}_f\delta\mathbf{q}_f\end{aligned} \tag{39}$$

where

$$\mathbf{M}_c = \left.\frac{\partial\mathcal{D}}{\partial\ddot{\mathbf{q}}_p}\right|_0, \mathbf{C}_c = \left.\frac{\partial\mathcal{D}}{\partial\dot{\mathbf{q}}_p}\right|_0, \mathbf{K}_c = \left.\frac{\partial\mathcal{D}}{\partial\mathbf{q}_p}\right|_0 \in \mathbb{R}^{p\times m},$$
$$\mathbf{M}_f = \left.\frac{\partial\mathcal{D}}{\partial\ddot{\mathbf{q}}_f}\right|_0, \mathbf{C}_f = \left.\frac{\partial\mathcal{D}}{\partial\dot{\mathbf{q}}_f}\right|_0, \mathbf{K}_f = \left.\frac{\partial\mathcal{D}}{\partial\mathbf{q}_f}\right|_0 \in \mathbb{R}^{p\times p},$$

and note that $\mathbf{C}_c = \mathbf{0}_{p\times m}$ and $\mathbf{C}_f = \mathbf{0}_{p\times p}$ because the system model does not have any elements with viscous damping.

To compose the linearized internal dynamics, Eq. (39), as only the function of free perturbation variables $\delta\mathbf{q}_f$, $\delta\dot{\mathbf{q}}_f$, and $\delta\ddot{\mathbf{q}}_f$, the relation between the two perturbation variables is identified by linearizing the constraint equations, Eq. (7), with the same linearization method as above

$$\Phi_0 = \Phi(\mathbf{q}_0,\boldsymbol{\ell}_0) + \left.\frac{\partial\Phi}{\partial\mathbf{q}_c}\right|_0\delta\mathbf{q}_c + \left.\frac{\partial\Phi}{\partial\mathbf{q}_f}\right|_0\delta\mathbf{q}_f. \tag{40}$$

From Eq. (40), $\delta\mathbf{q}_c$, $\delta\dot{\mathbf{q}}_c$, and $\delta\ddot{\mathbf{q}}_c$ can be obtained as

$$\delta\mathbf{q}_c = \Psi\delta\mathbf{q}_f \tag{41a}$$
$$\delta\dot{\mathbf{q}}_c = \Psi\delta\dot{\mathbf{q}}_f \tag{41b}$$
$$\delta\ddot{\mathbf{q}}_c = \Psi\delta\ddot{\mathbf{q}}_f \tag{41c}$$

where

$$\Psi \triangleq -\left(\left.\frac{\partial\Phi}{\partial\mathbf{q}_c}\right|_0\right)^{-1}\left.\frac{\partial\Phi}{\partial\mathbf{q}_f}\right|_0 \in \mathbb{R}^{r\times p}. \tag{42}$$

By substituting Eq. (41) in Eq. (39), the linearized internal dynamics expressed in terms of only free perturbation variables can be obtained as

$$\mathcal{D}_0^*\left(\mathbf{q}_f,\dot{\mathbf{q}}_f,\ddot{\mathbf{q}}_f\right) = \mathbf{M}_f^*\delta\ddot{\mathbf{q}}_f + \mathbf{K}_f^*\delta\mathbf{q}_f = \mathbf{0} \tag{43}$$

where

$$\mathbf{M}_f^* = \mathbf{M}_p\Psi + \mathbf{M}_f \in \mathbb{R}^{p\times p} \tag{44}$$
$$\mathbf{K}_f^* = \mathbf{K}_p\Psi + \mathbf{K}_f \in \mathbb{R}^{p\times p}. \tag{45}$$

Thus, the natural frequencies of the UCCDPR can be obtained as $\omega_n = \sqrt{\text{eigenvalue}\left((\mathbf{M}_f^*)^{-1}\mathbf{K}_f^*\right)}$ and they depend on equilibrium pose of the EE, $\mathbf{q}_0$.

V. DESIGN OF INPUT-SHAPER

Input shaping is a feed-forward control technique that suppresses the vibration of an oscillating system by modifying the original command input signal through a sequence of impulse signals designed based on the natural frequency of the target system [37], [38]. The modified command signal, which has a vibration canceling characteristic, is generated through convolution with the original command and sequence of impulse signals. The sequence of impulses can be expressed by

$$I(t) = \sum_{j=1}^{v} M_j\delta(t-\tau_j) \tag{46}$$

where $\delta(\cdot)$ represents the Dirac delta function, v is the number of impulses demanded to reduce the oscillations and M_j is the amplitude of jth pulse at time τ_j. All of the M_j is a non-zero value, and their sum is 1, that is, $\sum M_j = 1$.

In this work, two input sharper is used to suppress the residual vibrations caused by the free DOF of the UCCDPR and to compare their oscillation reducing performance: one is designed based on the Zero-Vibration (ZV) method and the other is designed based on the Zero-Vibration and Derivative (ZVD) method. Note that the input shaper based on ZVD is significantly more robust to modeling errors than the ZV shaper and the number of impulses is $v = 2$ for ZV-based and $v = 3$ for ZVD-based.

And, since UCCDPR has p vibration modes, an impulse signal is generated as

$$I_k(t) = \sum_{j=1}^{v} M_{k,j}\delta(t-\tau_{k,j}), \quad (k = 1,\cdots,p) \tag{47}$$

where

$$\text{ZV:}\begin{bmatrix}M_{k,j}\\ \tau_{k,j}\end{bmatrix} = \begin{bmatrix}\frac{K_k}{1+K_k} & \frac{1}{1+K_k}\\ 0 & \frac{\pi}{\omega_{d,k}}\end{bmatrix}, \tag{48a}$$

$$\text{ZVD:}\begin{bmatrix}M_{k,j}\\ \tau_{k,j}\end{bmatrix} = \begin{bmatrix}\frac{K_k^2}{(1+K_k)^2} & \frac{K}{(1+K_k)^2} & \frac{1}{(1+K_k)^2}\\ 0 & \frac{\pi}{\omega_{d,k}} & \frac{2\pi}{\omega_{d,k}}\end{bmatrix} \tag{48b}$$

Here, $K_k = \exp(-\zeta_k\pi/\sqrt{1-\zeta_k^2})$ and $\omega_{d,k} = \omega_{n,k}\sqrt{1-\zeta_k^2}$. ζ_k, $\omega_{d,k}$ and $\omega_{n,k}$ denote the damping ratio, damped natural frequency, and natrual frequency of kth mode, respectively. Eq. (48) means that each amplitude of $I_k(t)$ is determined depending on the dampling ratio ζ_k only and each time of $I_k(t)$ is decided by the damped natural frequency $\omega_{d,k}$.

By convoluting all the impulse signals in Eq. (47), the multi-mode input shaper can be designed:

$$IS(t) = I_1(t) * \cdots * I_p(t). \tag{49}$$

where the symbol $*$ denotes the convolution. And the total number of the impulses of the multi-mode input shaper for p-mode system is v^p.

Fig. 3 shows the process of modifying the original command input signal to an input signal for vibration suppression

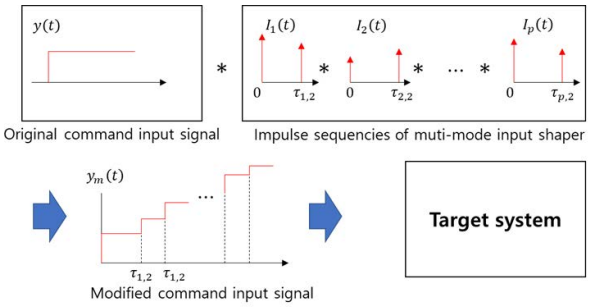

FIGURE 3. Process of modifying the original command signal based on multi-mode ZV shaper.

using the p-mode input shaper. The modified command signal, $y_m(t)$, is generated by convoluting the original command signal, $y(t)$, with the multi-mode input shaper, $IS(t)$, that is:

$$y_m(t) = IS(t) * y(t). \tag{50}$$

In case of UCCDPR systems, the number of modes is equal to the number of the free state variables of the EE. And all damping ratios are zero since the system in Eq. (43) does not have damping, thus K_k is 1 and the damped natrual frequency, ω_d, is equal to the natural frequency, ω_n.

VI. SIMULATIONAL AND EXPERIMENTAL VERIFICATIONS

To validate the effectiveness and performance of the proposed method, computer simulations were carried out by utilizing commercial software, Matlab®. In addition, experiments were conducted on a 3-dimensional UCCDPR with a 4-cable prototype.

The control procedure of the overall system applied for the simulations as well as the hardware system is shown in Fig. 4. The original position trajectory of the EE, $\mathbf{p}_d$, is designed and passes through the input shaper, where it is adjusted as the modified position trajectory, $\mathbf{p}_m$, for preventing the occurrence of unwanted vibrations. Based on the modified position trajectory, each cable length, $\mathbf{L}_d$, is calculated through the EQBT generator based on the proposed method expressed in Section IV-A. And the desired angular trajectory of a $\Theta_m^d(t)$ is computed from the trajectory of desired cable length based on the model of the motors combined with the winches. Finally, to make each motor angle track the desired one, a PID controller is applied. The control gains for all the motors are set to be identical.

A. SIMULATIONS

In the simulations, a 4-cable UCCDPR model, which was modeled based on the UCCDPR used in the experiments shown in Fig. 5, was used. The main parameters of each CDPR are listed in Tables 1 and 2. The cables used in the simulation are assumed to have none of the compliance, sagging, and damping. And it is assumed that the kinetics of each winch is ignored and that there is no friction between each cable and its pulley.

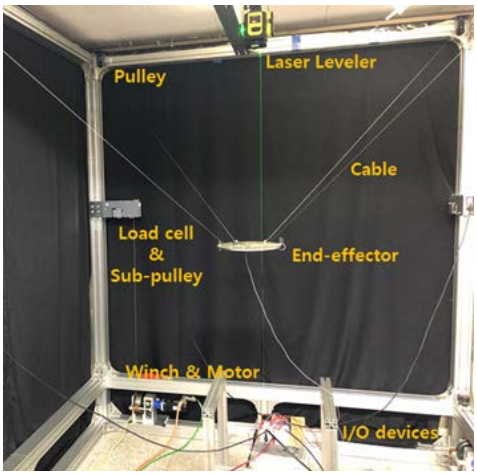

FIGURE 4. Block diagram of UCCDPR control system.

TABLE 1. Parameters of 4-cable UCCDPR system used in the simulations and experiments (unit: meter).

i	1	2	3	4
$\mathbf{a}_i$	$\begin{bmatrix}0\\0\\2\end{bmatrix}$	$\begin{bmatrix}2\\0\\2\end{bmatrix}$	$\begin{bmatrix}2\\2\\2\end{bmatrix}$	$\begin{bmatrix}0\\2\\2\end{bmatrix}$
$\mathbf{r}_i^E$	$\begin{bmatrix}-0.0575\\-0.1\\0\end{bmatrix}$	$\begin{bmatrix}0.0575\\-0.1\\0\end{bmatrix}$	$\begin{bmatrix}0.0575\\0.1\\0\end{bmatrix}$	$\begin{bmatrix}-0.0575\\0.1\\0\end{bmatrix}$

TABLE 2. Parameters of the EE used in the simulations and experiments.

description	specification
payload radius [m]	0.115
payload mass[kg]	0.795
$\boldsymbol{\zeta}^E$ [m]	$\begin{bmatrix}0 & 0 & 0.005\end{bmatrix}^T$
payload moment of inertia $\mathbf{I_{xx}}$ [kg·m^2]	3.104×10^{-3}
payload moment of inertia $\mathbf{I_{yy}}$ [kg·m^2]	3.104×10^{-3}
payload moment of inertia $\mathbf{I_{zz}}$ [kg·m^2]	6.204×10^{-3}

B. SIMULATION I: MAP OF EQUILIBRIUM CONFIGURATIONS

In order to show that it is possible to obtain the equilibrium configuration over all positions within the workspace of the UCCDPR through the proposed method, finding the equilibrium configuration for positions of the EE was carried out. Figs. 6 and 7 show how the orientation angle, each cable length, and tension magnitude of the 4-cable UCCDPR system change as the EE changes its horizontal position at $z = 1$ m. As shown in Fig. 6, the tilting angle of the EE on a horizontal plane increases rapidly as the EE approaches the edge of the workspace. Fig. 7 shows the length and tension magnitude of each cable of the 4-cable UCCDPR, and it can be seen that the length and tension of each cable are inversely proportional to each other. This phenomenon occurs because the shorter the length of the cable, the greater the angle between the cable vector $\mathbf{l}_i$ and the gravitational force. Note that the map ($\mathbf{p}_0 \rightarrow \mathbf{X}_u$) depends on the inertial mass of the EE and the cable connecting points on the EE.

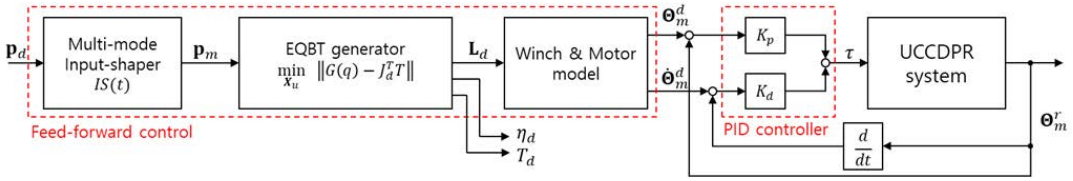

FIGURE 5. 4-cable UCCDPR system used in the experiments.

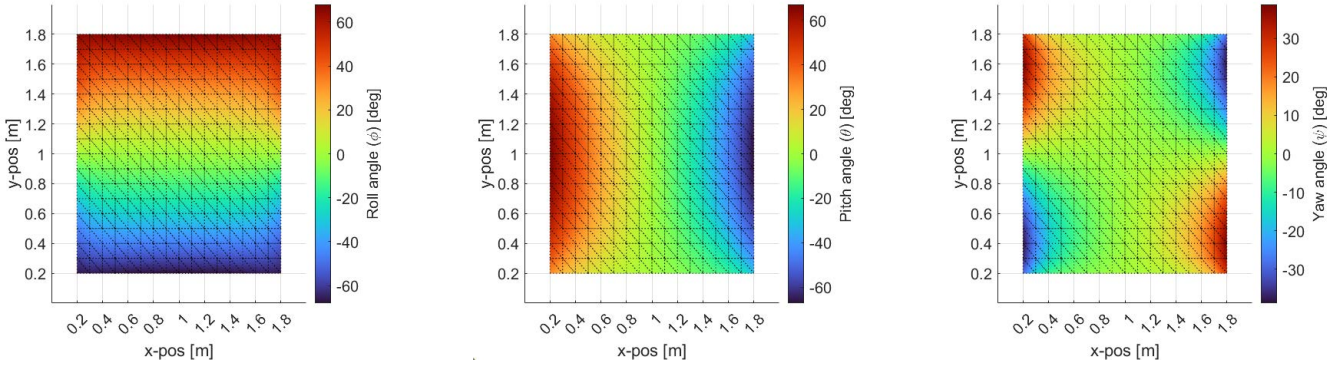

(a) Roll angle (b) Pitch angle (c) Yaw angle

FIGURE 6. Orientation angles of the EE at stable equilibrium state on a horizontal plane at $z = 1$ m.

C. SIMULATION II: PERFORMANCE OF TRAJECTORY GENERATED THROUGH THE PROPOSED METHOD

To highlight the effectiveness of the proposed method in improving trajectory tracking and oscillation suppression, simulations were performed based on a 4-cable UCCDPR system shown in Fig. 5. Note that changes in the orientation of the EE and the natural frequencies of the UCCDPR inevitably occur as the EE moves and that the amount of their changes during the motion depends on the trajectory of the EE. Therefore, to show the performance of the proposed method for each of the large and small changes in orientation and natural frequency, a set of simulations were carried out using two different paths: one causing small changes in the orientation and natural frequency, which is Path 1, and the other causing relatively large ones, which is Path 2. These paths are shown in Fig. 8, which are described by

$$\mathbf{p}_d(t) = \mathbf{p}_0 + \begin{bmatrix} R_x(\cos\theta_p(t) - 1) \\ R_y \sin\theta_p(t) \\ R_z(\cos\theta_p(t) - 1) \end{bmatrix} \tag{51}$$

where $\mathbf{p}_0$ is the initial position of the EE. For Path 1, $\mathbf{p}_0 = [1.35, 1, 1]^T$, $R_x = R_y = 0.35$ and $R_z = 0$. For Path 2, $\mathbf{p}_0 = [1.5, 1, 1.5]^T$, $R_x = R_y = R_z = 0.5$. All the units used here are meters. The orientation angles and natural frequencies at equilibrium on each path versus θ_p are shown in Figs. 9 and 10.

The performance in vibration suppression of the input-shaped trajectories was compared for different angular velocities $\dot{\theta}_p(t)$: one with a constant angular velocity, one with a trapezoidal angular velocity, and ZV and ZVD shaper-based trajectories.

1) Constant velocity (CV): angle $\theta_p(t)$ in Eq. (51) is designed with

$$\theta_p(t) = \frac{2\pi}{T_{f,CV} - T_0} t, \quad T_0 \le t \le T_{f,CV} \tag{52}$$

where T_0 and $T_{f,CV}$ denote the times at which the motion starts and ends, respectively.

2) Trapezoidal velocity (TV): The velocity of $\theta_p(t)$ in Eq. (51) is designed as

$$\dot{\theta}_p(t) = \begin{cases} \dfrac{2\pi}{(T_{f,CV} - T_0)T_d}(t - t_0), & T_0 \le t < T_0 + T_d \\ \dfrac{2\pi}{T_{f,CV} - T_0}, & T_0 + T_d \le t < T_{f,CV} \\ \dfrac{2\pi}{(T_{f,CV} - T_0)}(1 - \frac{t - T_{f,CV}}{T_d}), & T_{f,CV} \le t < T_{f,TV} \end{cases} \tag{53}$$

where T_d is the time interval for acceleration and deceleration, and it was set to be the same as the delay time occurring in the ZV shaper to compare performance with the ZV shaper under the same condition.

3) ZV and ZVD shaper-based trajectory:

$$\mathbf{p}_m(t) = IS_{ZV}(t) * \mathbf{p}_d^*(t) \tag{54}$$

$$\mathbf{p}_m(t) = IS_{ZVD}(t) * \mathbf{p}_d^*(t). \tag{55}$$

where $\mathbf{p}_d^*(t)$ is the CV trajectory.

The EE stays at position $\mathbf{p}_0$ for 1 second, before it starts moving along the given trajectory for the next 5 seconds ($T_{f,CV}$=6 s) in the case of CV, 5.672 seconds ($T_{f,CV}$=6.672 s) in the case of TV for Path 1, and 5.4 seconds ($T_{f,CV}$=6.4 s) in the case of TV for Path 2. Note that the time delays T_d caused

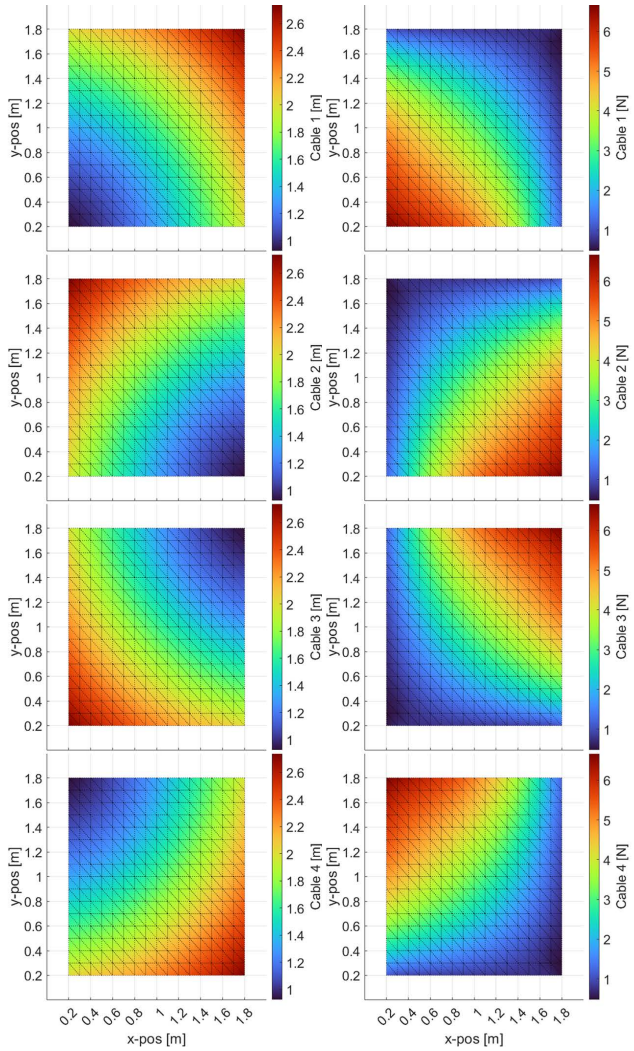

(a) Each cable length (b) Each cable tension

FIGURE 7. Each cable length and tension at the stable equilibrium states on a horizontal plane at $z = 1$ m.

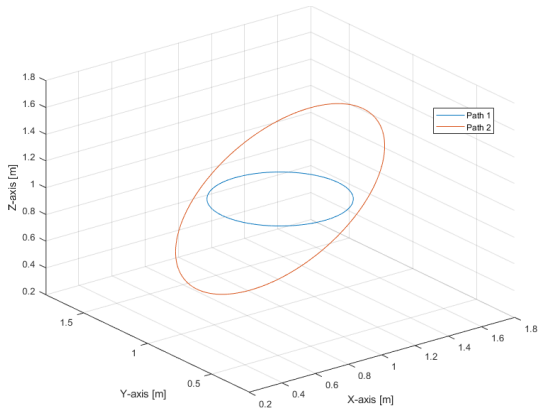

FIGURE 8. Two circular paths used in the simulations and the experiments. Path 1 lies on a horizontal plane (Z=1) and Path 2 on a tilted one.

by the ZV shaper were 0.672 s for Path 1 and 0.4 s for Path 2, respectively.

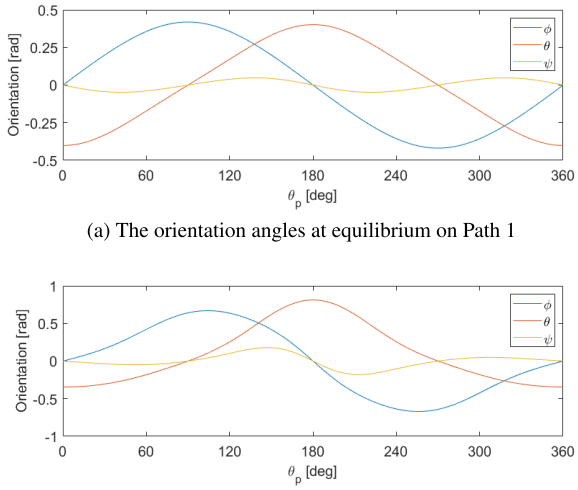

(a) The orientation angles at equilibrium on Path 1

(b) The orientation angles at equilibrium on Path 2

FIGURE 9. Orientation angles at equilibrium on each path.

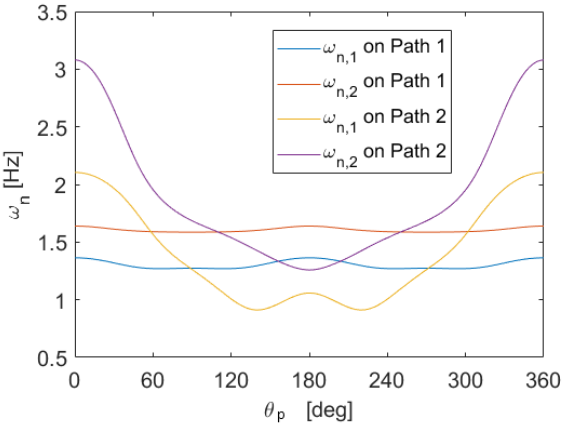

FIGURE 10. Natural freqeuncies along the path.

The desired orientation trajectory of the EE is generated as the EQBT, generated by obtaining the orientation trajectory based on the equilibrium configuration on the given position trajectory through the proposed method explained in Section IV-A. And orientation angles for a linear orientation-based trajectory (LOBT) used to compare with EQBT are generated as

$$\boldsymbol{\eta}(t) = \boldsymbol{\eta}(T_0) + \frac{t}{T_f - T_0}(\boldsymbol{\eta}(T_f) - \boldsymbol{\eta}(T_0)), \quad T_0 \le t < T_f \tag{56}$$

where T_f denotes the time at which the EE motion ends. Note that the positional trajectories of the EQBT are the same as LOBT's position trajectory, but not the orientation trajectories.

The simulations were carried out using LOBTs and EQBTs, designed to have 4 velocity types explained above for each path, and their results were compared.

1) RESULTS ON PATH 1

In the first simulations, in the case of the path causing the small changes of the orientation angles and natural

TABLE 3. RMS of residual oscillations for Path 1.

Oscillation Type	Trajetory Type	CV	TV	ZV	ZVD
position [mm]	LOBT	9.64	1.46	0.73	0.41
	EQBT	4.22	1.35	0.54	0.41
orientation [deg]	LOBT	8.17	1.26	0.62	0.36
	EQBT	3.62	1.19	0.46	0.36

TABLE 4. RMS of tracking error for Path 1.

Oscillation Type	Trajetory Type	CV	TV	ZV	ZVD
position [mm]	LOBT	39.26	34.80	33.77	31.14
	EQBT	19.44	5.56	4.69	3.99
orientation [deg]	LOBT	30.20	26.14	25.66	23.93
	EQBT	13.61	3.78	3.08	2.53

frequencies, the focus was on how the performance on the trajectory tracking is improved when the EQBT is used compared with LOBT. And when EQBT is used with an input shaper, it is also checked how much the vibration suppression effect is improved.

As shown in Figs. 11 and 12, which are the results of using LOBT and EQBT, respectively, the residual oscillations could be significantly subsided using only the input shaper, whether LOBT or EQBT was used. And the performance in the residual oscillation suppression in all simulations was best when the ZVD shaper was used, followed by when using the ZV shaper. This result shows that the ZVD shaper is more robust than the ZV shaper in the case that the change of frequencies occurs on the path. The RMS values of the residual oscillations were measured for 10 seconds after completing a circular motion and summarized in Table 3. Although using only the input shaper in LOBT can suppress the residual vibration, using EQBT with the ZV shaper was able to suppress the residual vibrations by 26% more compared to using LOBT with the ZV shaper. Besides, even for CV and TV, using EQBT produced less residual vibration than CV and TV of LOBT.

And, in the trajectory tracking performance, all the results with the EQBT showed improved performance compared to all the results with the LOBT. In particular, despite using the same position trajectory in both LOBT and EQBT, the position trajectory was followed well when using EQBT, while the performance in the position tracking was poor when using LOBT. These results are revealed by just comparing Figs. 11c and 12c. In this simulation, the assigned z-axis position trajectory was the time-invariant i.e., $z = 1$ m for all the simulation time. As shown in Figs. 11c and 12c, using LOBT did not track the z-axis trajectory, but using EQBT could follow the given trajectory. The RMS values on the tracking error, measured for the time for a single turn of circular motion, are listed in Table 2. In the cases of TV, ZV, and ZVD of EQBT, the tracking errors were reduced by more than 85% compared to the case of TV, ZV, and ZVD of LOBT.

2) RESULTS ON PATH 2

For a motion along Path 2, large changes in the orientation angles and natural frequencies are caused as shown in Figs. 9 and 10. Thus, additional simulations were conducted to see how these changes in orientation and frequency affect the transient and residual oscillations and tracking performance

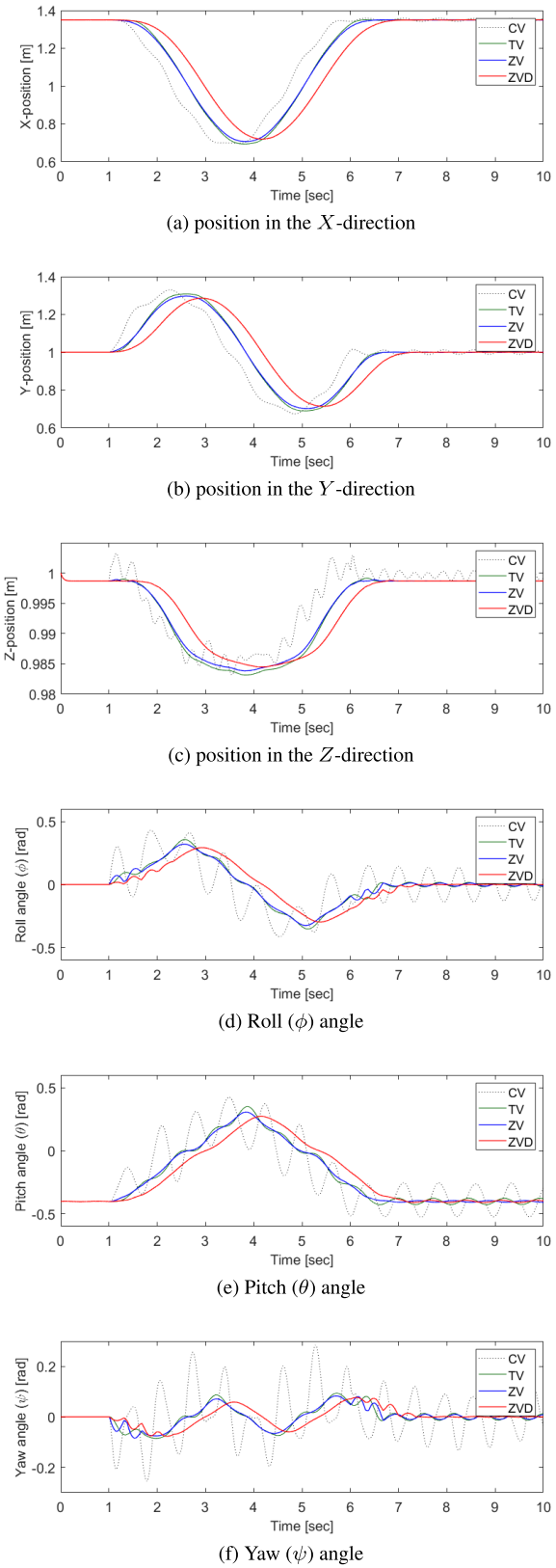

(a) position in the X-direction

(b) position in the Y-direction

(c) position in the Z-direction

(d) Roll (ϕ) angle

(e) Pitch (θ) angle

(f) Yaw (ψ) angle

FIGURE 11. Simulation results for the LOBT for Path 1.

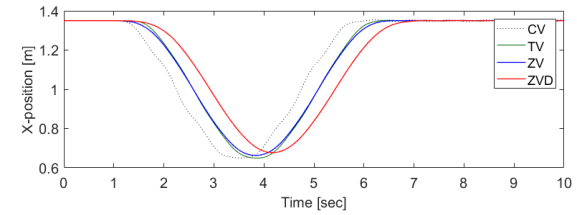

(a) position in the X-direction

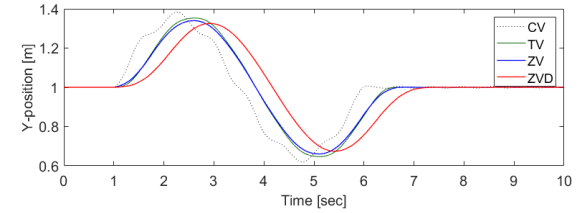

(b) position in the Y-direction

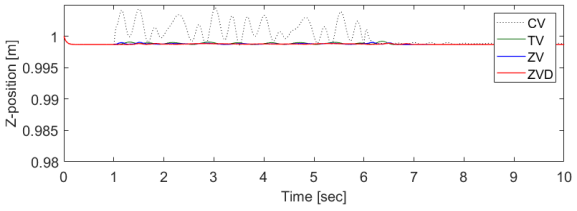

(c) position in the Z-direction

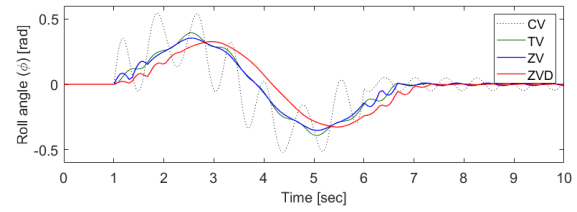

(d) Roll (ϕ) angle

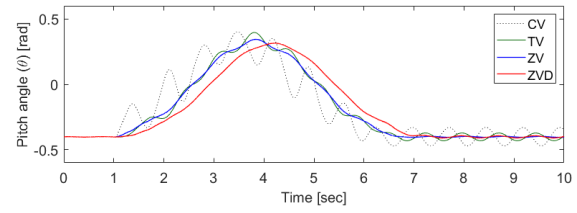

(e) Pitch (θ) angle

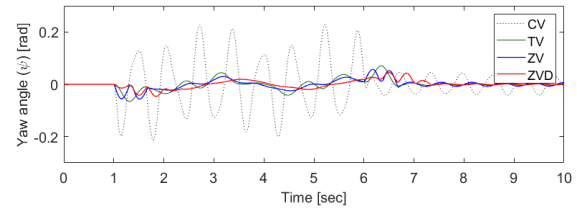

(f) Yaw (ψ) angle

FIGURE 12. Simulation results for the EQBT the Path 1.

of EE and to see how effective it is to use EQBT in the path where these changes occur significantly.

TABLE 5. RMS of residual oscillations for Path 2.

Oscillation Type	Trajetory Type	CV	TV	ZV	ZVD
position [mm]	LOBT	2.99	2.34	1.84	1.65
	EQBT	2.78	1.62	0.46	0.43
orientation [deg]	LOBT	5.23	4.47	3.77	3.37
	EQBT	4.06	2.39	0.70	0.78

TABLE 6. RMS of tracking error for Path 2.

Oscillation Type	Trajetory Type	CV	TV	ZV	ZVD
position [mm]	LOBT	59.47	56.31	55.24	52.36
	EQBT	12.93	8.11	7.73	7.32
orientation [deg]	LOBT	33.86	31.81	31.34	29.89
	EQBT	9.53	4.90	4.51	4.23

In the case of Path 2, as shown in Fig. 13, there was a limit to suppressing the residual oscillation of the EE by using LOBT with the input shaper even using the ZVD shaper. Since the natural frequencies used to design the input shaper are the value at the start point only, i.e., constant values, the vibration suppression effect through the input shaper is small in a path where large changes in natural frequencies are caused, such as Path 2. However, looking at the results shown in Fig. 14, it could be confirmed that the residual oscillations were significantly subsided as well as transitional oscillations caused during circular motion in all the cases of using the EQBT. The RMS values on the residual oscillations measured for 10 seconds after completing a circular motion are listed in Table 5. It is noteworthy that even in the case of TV of EQBT, residual vibration occurs less than in the case of LOBT using ZVD. Also, despite the significant changes in orientation angles and natural frequencies, residual oscillations were substantially subdued by more than 75% when the EQBT was used with input shaper compared to using LOBT with input shaper.

In addition, using EQBT could improve the performance in trajectory tracking compared to using LOBT. In all the cases of using EQBT, the tracking errors, measured for the time for a single turn of circular motion, declined by more than 85% compared to all the cases of using LOBT, and that are summarized in Table 6. These results show how effective the use of EQBT in the UCCDPR system is in suppressing unwanted oscillatory motions and in reducing tracking errors.

D. EXPERIMENTS

Hardware experiments were carried out with the UCCDPR system with 4 cables, shown in Fig. 5. Stainless steel cables with 1 mm diameter were used and the length was controlled by an AC servomotor (Beckhoff, AM3024) with an AC servo driver (Beckhoff, AX5203). A loadcell (Bongshin, OBUH-10) to measure the cable tension was installed at each of the sub-pulleys. To measure the orientation of the EE, an IMU sensor (MocroStrain, 3DM-GX5-25) was installed on the EE. And a laser leveler (Sincon, CU-900T) and a laser range sensor (Magpie, VH-80) were used to set the initial position of the EE and to measure the position when the EE is stationary.

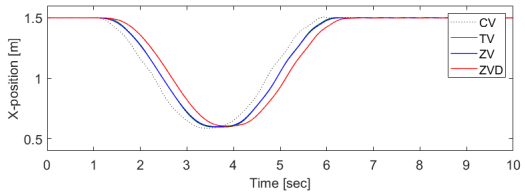

(a) position in the X-direction

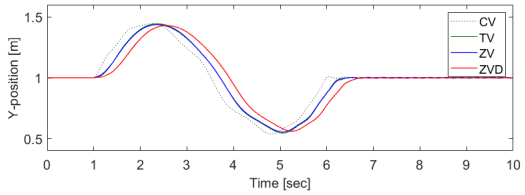

(b) position in the Y-direction

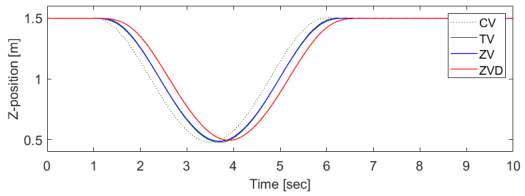

(c) position in the Z-direction

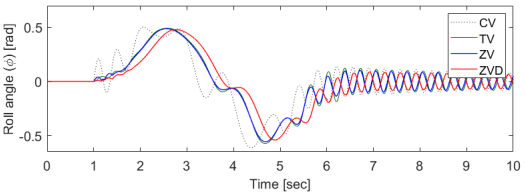

(d) Roll (ϕ) angle

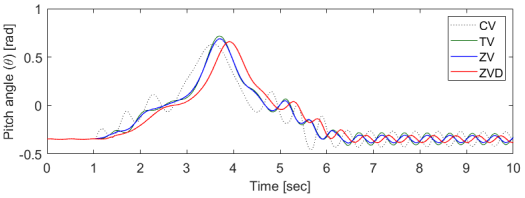

(e) Pitch (θ) angle

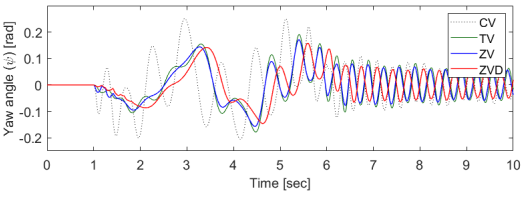

(f) Yaw (ψ) angle

FIGURE 13. Simulation results for the LOBT for Path 2.

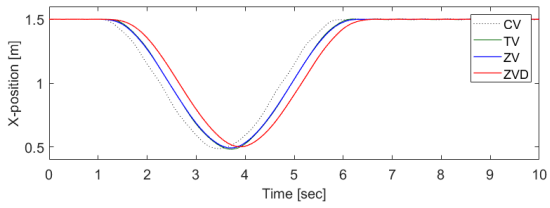

(a) position in the X-direction

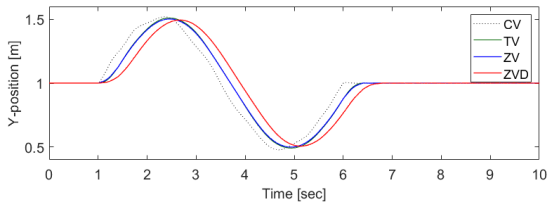

(b) position in the Y-direction

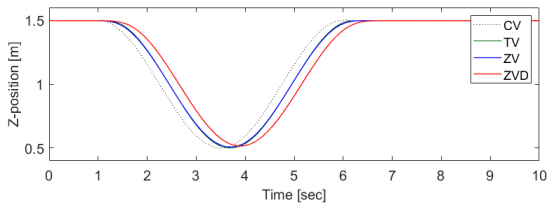

(c) position in the Z-direction

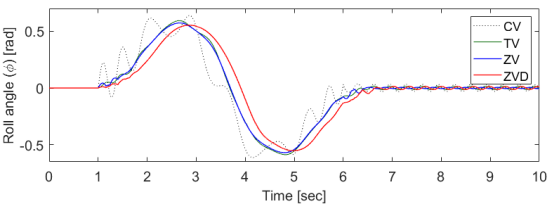

(d) Roll (ϕ) angle

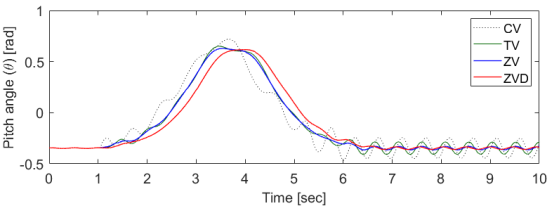

(e) Pitch (θ) angle

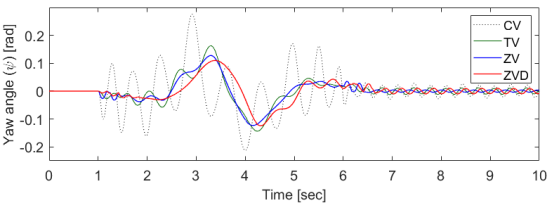

(f) Yaw (ψ) angle

FIGURE 14. Simulation results for the EQBT for Path 2.

E. EXPERIMENT I: PERFORMANCE OF TRAJECTORY GENERATED THROUGH THE PROPOSED METHOD

The experiments were conducted using the paths and trajectories used in the simulations and all the data on the orientation of the EE were measured with the IMU sensor attached to the EE. And the experiment results for both Path 1 and Path 2 were similar to the simulation results.

In the case of experiments on Path 1, comparing the results of using LOBT and EQBT shown in Figs. 15 and 16, it can be seen that all the cases of using EQBT suppressed residual oscillations of the EE compared to all the cases using LOBT.

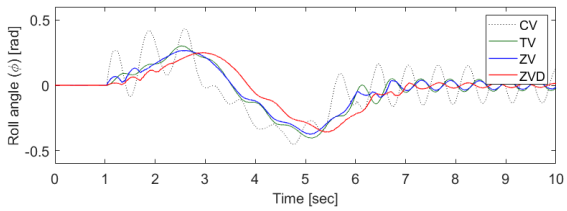

(a) Roll angle

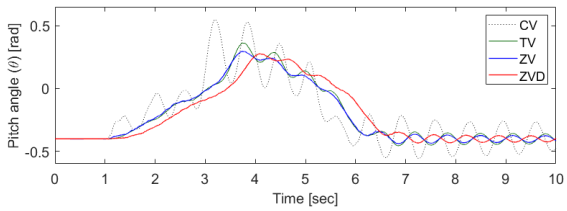

(b) Pitch angle

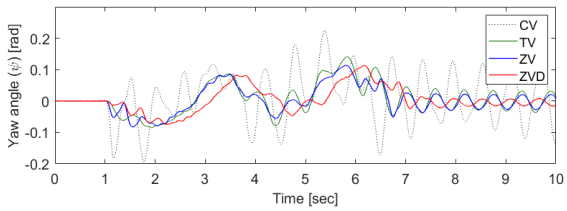

(c) Yaw angle

FIGURE 15. Experiment results for the LOBT for Path 1.

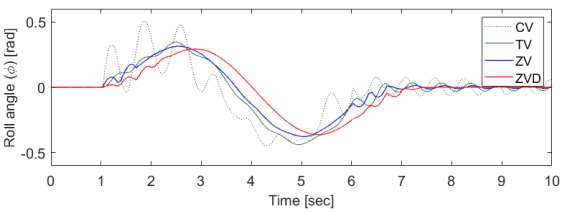

(a) Roll angle

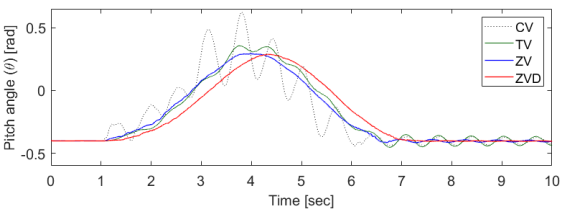

(b) Pitch angle

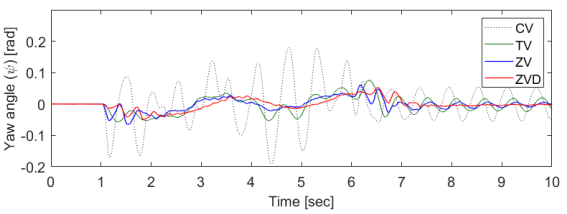

(c) Yaw angle

FIGURE 16. Experiment results for the EQBT for Path 1.

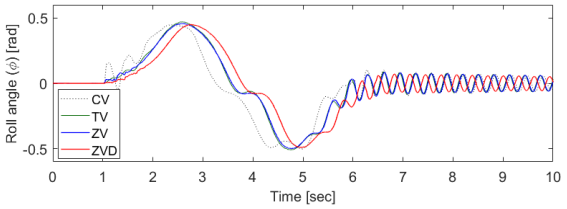

(a) Roll angle

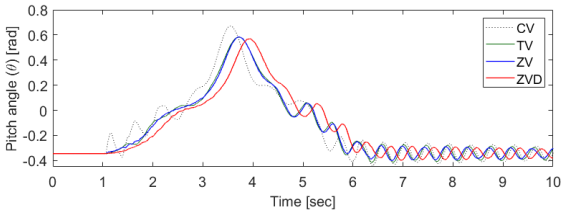

(b) Pitch angle

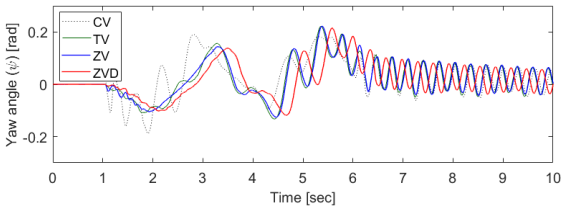

(c) Yaw angle

FIGURE 17. Experiment results for the LOBT for Path 2.

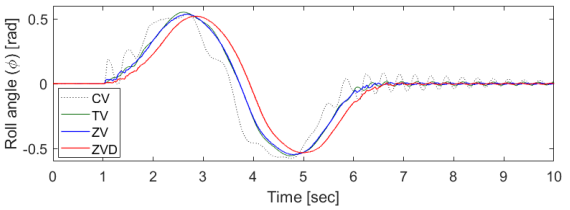

(a) Roll angle

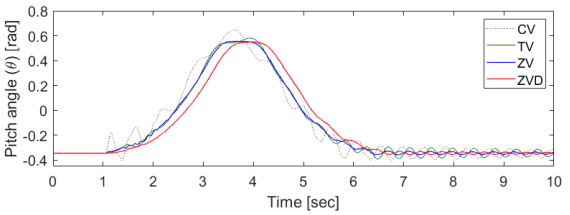

(b) Pitch angle

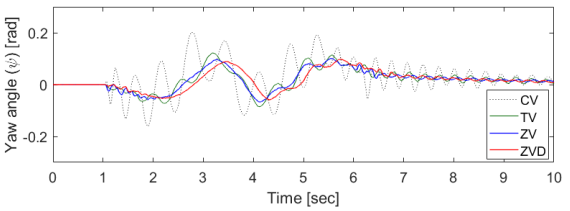

(c) Yaw angle

FIGURE 18. Experiment results for the EQBT for Path 2.

In particular, the use of only the TV of EQBT could suppress residual vibration to a level equivalent to that of ZV of LOBT, and in the case of using EQBT with the input shaper, there was almost no residual vibration occurred. As clearly

TABLE 7. RMS of the tracking error and residual oscillations on the orientation of the EE in the experiments of motion along Path 1 (unit: degrees).

		CV	TV	ZV	ZVD
Tracking error	LOBT	30.63	28.08	27.14	26.43
	EQBT	12.75	6.53	4.94	4.78
Residual oscillation	LOBT	7.95	2.31	1.61	1.00
	EQBT	2.99	1.72	0.56	0.18

TABLE 8. RMS of the tracking error and residual oscillations on the orientation of the EE in the experiments of motion along Path 2 (unit: degrees).

		CV	TV	ZV	ZVD
Tracking error	LOBT	32.63	31.60	31.23	30.85
	EQBT	9.56	7.38	7.11	6.92
Residual oscillation	LOBT	3.84	3.55	3.33	2.87
	EQBT	2.43	1.35	0.66	0.62

shown in the circular motion parts of Figs. 15 and 16, the transition vibration was also reduced in all cases of EQBT compared to the results of LOBT. The tracking performance and residual vibration suppression performance of EQBT with input shaper showed more than 80% improvement compared to LOBT with input shaper, which is summarized in Table 7.

Looking at the results for Path 2, it is better to see the difference in performance between using LOBT and using EQBT. As can be seen in Figs. 17, and 18, all the results with EQBT were better than any of those with LOBT, even ZVD. This shows how good the use of EQBT can be in the case of paths with significant changes in natural frequency and posture on the path. In Path 2, the tracking performance and residual vibration suppression performance of the input-shaped EQBT showed an improvement of more than 77% compared to those of the input-shaped LOBT, which is summarized in Table 8.

By the way, there is a difference between experimental and simulation results on both Path 1 and Path 2. The amplitude of the residual vibrations generated in the experiment is smaller than the amplitude generated in the simulation. This difference is caused by energy loss elements in the hardware which were neglected in the simulation model, such as pulley friction and damping/friction in the cables.

VII. CONCLUSION

This paper proposed a method for finding the equilibrium configuration of general under-constrained cable-driven parallel robots. The cable length and tension, and orientation of the EE could be obtained for the UCCDPR to be in a stable and static equilibrium configuration at the given EE position by solving the optimization problem, which has the objective function as the 2-norm of statics with the constraints concerning the cable tension and the orientation of the EE. Through the proposed method, even in UCCDPR employing more than 4 cables, EQBT could be generated considering the orientation of the EE even if only the position trajectory of the EE was assigned. In addition, the natural frequencies of the UCCDPR were analyzed in the entire workspace by linearizing the internal dynamics of UCCDPR around the equilibrium point obtained by the proposed method, and an input-shaper was designed based on the natural frequencies. The trajectory tracking performance was significantly improved by using the input-shaped EQBT as well as the suppression of the transitional and residual oscillational motion. By conducting simulations and experiments comparing the performance of EQBT and LOBT, it was verified how effective it is to use EQBT in the UCCDPR system.

APPENDIX A
LENGTH OF CABLE

For convenience, for all, use $\hat{\mathbf{i}}$, $\hat{\mathbf{j}}$, and $\hat{\mathbf{k}}$ for $[1\ 0\ 0]^T$, $[0\ 1\ 0]^T$, and $[0\ 0\ 1]^T$. Note that $\mathbf{u}_i$, $\mathbf{w}_i$, $\mathbf{l}_i$, and $\mathbf{s}_i$ are coplanar vectors lying on the pulley plane i. The vector $\mathbf{l}_i$ in Eq. 3 can be expressed with respect to $\{A_i\}$ by multiplying both sides by $\mathbf{R}_i^T$:

$$\mathbf{l}_i^{A_i} = \mathbf{u}_i^{A_i} + \mathbf{w}_i^{A_i} - \mathbf{s}_i^{A_i} \tag{57}$$

where

$$\mathbf{u}_i^{A_i} = r_i\hat{\mathbf{i}} \tag{58}$$

$$\mathbf{w}_i^{A_i} = r_i[-\cos\theta_i\ 0\ \sin\theta_i]^T \tag{59}$$

$$\mathbf{s}_i^{A_i} = \mathbf{R}_i^T\mathbf{s}_i. \tag{60}$$

Because all the vectors in Eq. (57) exist on the pulley plane, their y-components must be zero. From this fact, the y-component of $\mathbf{s}_i^{A_i}$ can be expressed as follows:

$$\begin{aligned} 0 &= \mathbf{s}_i^{A_i}\cdot\hat{\mathbf{j}} \\ &= \mathbf{R}_{z_i}^T(\mathbf{R}_i^*)^T\mathbf{s}_i\cdot\hat{\mathbf{j}} \\ &= -\sin\gamma_i((\mathbf{R}_i^*)^T\mathbf{s}_i\cdot\hat{\mathbf{i}}) + \cos\gamma_i((\mathbf{R}_i^*)^T\mathbf{s}_i\cdot\hat{\mathbf{j}}). \end{aligned} \tag{61}$$

From Eq. (61), the swivel angle, γ_i, can be obtained as

$$\gamma_i = \text{atan2}\left((\mathbf{R}_i^*)^T\mathbf{s}_i\cdot\hat{\mathbf{i}},\ (\mathbf{R}_i^*)^T\mathbf{s}_i\cdot\hat{\mathbf{j}}\right). \tag{62}$$

And the wrap angle, θ_i, can be obtained using the condition that the edge of the pulley groove and the cable are in contact at point B_i. On the pulley plane, the edge of the pulley can be represented by

$$\left(x_i - \mathbf{u}_i^{A_i}\cdot\hat{\mathbf{i}}\right)^2 + \left(z_i - \mathbf{u}_i^{A_i}\cdot\hat{\mathbf{k}}\right)^2 = r_i^2 \tag{63}$$

and the line passing through point C_i and contacting the edge of the pulley groove can be expressed as follows:

$$z_i - \mathbf{s}_i^{A_i}\cdot\hat{\mathbf{k}} = d\left(x_i - \mathbf{s}_i^{A_i}\cdot\hat{\mathbf{i}}\right) \tag{64}$$

where d means the gradient of the line and it is

$$d = \frac{-\gamma_b \pm \sqrt{\gamma_b^2 - 4\gamma_a\gamma_c}}{2\gamma_a} \tag{65}$$

where

$$\gamma_a = r_i^2 - \left((\mathbf{u}_i^{A_i} - \mathbf{s}_i^{A_i}) \cdot \hat{\mathbf{i}}\right)^2$$
$$\gamma_b = -2(\mathbf{u}_i^{A_i} - \mathbf{s}_i^{A_i}) \cdot (\mathbf{u}_i^{A_i} - \mathbf{s}_i^{A_i})$$
$$\gamma_c = r_i^2 + \left((\mathbf{u}_i^{A_i} - \mathbf{s}_i^{A_i}) \cdot \hat{\mathbf{k}}\right)^2.$$

Note that the line expressed in Eq. (64) mathces the vector $\mathbf{l}_i$. And two gradients are provided from Eq. (65), and it means that the two tangent line satisfying both passing through point C_i and contacting on the pulley exist. In this research, the gradient with a larger absolute value is used because each pulley is installed at a higher position than the position of EE. By finding the point of tangency between Eqs. (63) and (64), the x and z positions of B_i on the pulley plane can be obtained by

$$B_{i,x}^{A_i} = \frac{(d^2\mathbf{s}_i^{A_i} + \mathbf{u}_i^{A_i}) \cdot \hat{\mathbf{i}} + d(\mathbf{u}_i^{A_i} - \mathbf{s}_i^{A_i}) \cdot \hat{\mathbf{k}}}{d^2 + 1} \tag{66}$$
$$B_{i,z}^{A_i} = d(B_{i,x}^{A_i} - \mathbf{s}_i^{A_i} \cdot \hat{\mathbf{i}}) + \mathbf{s}_i^{A_i} \cdot \hat{\mathbf{k}} \tag{67}$$

and note that $B_{i,y}^{A_i}$ is zero. From Eqs. (66) and (67), the vector $\mathbf{w}_i^{A_i}$ can be obtained as follows:

$$\mathbf{w}_i^{A_i} = \begin{bmatrix} B_{i,x}^{A_i} \\ 0 \\ B_{i,z}^{A_i} \end{bmatrix} - \mathbf{u}_i^{A_i}. \tag{68}$$

Thus, the wrap angle θ_i can be calculated by using the relation of the angle between $\mathbf{u}_i$ and $\mathbf{w}_i$.

$$\theta_i = \text{acos}\frac{-\mathbf{u}_i \cdot \mathbf{w}_i}{\|\mathbf{u}_i\|\|\mathbf{w}_i\|}. \tag{69}$$

As a consequence, the length of cable i from point C_i to point A_i is

$$L_i = r_i\theta_i + \ell_i. \tag{70}$$

APPENDIX B
KINEMATIC JACOBIAN

The relation of the rate of change between cable length and EE pose can be described by differentiating the kinematic constraints, $\ell_i^2 - \mathbf{l}_i^T\mathbf{l}_i = 0$, in Eq. (7):

$$\dot{\ell}_i = \hat{\mathbf{l}}_i^T\dot{\mathbf{l}}_i, \tag{71}$$

where $\hat{\mathbf{l}}_i = \mathbf{l}_i/\|\mathbf{l}_i\|$ and

$$\mathbf{l}_i = \mathbf{a}_i + \mathbf{R}_i\mathbf{u}_i^{A_i} + \mathbf{R}_i\mathbf{w}_i^{A_i} - \mathbf{c}_i \tag{72}$$
$$\dot{\mathbf{l}}_i = \dot{\mathbf{R}}_i\left(\mathbf{u}_i^{A_i} + \mathbf{w}_i^{A_i}\right) + \mathbf{R}_i\dot{\mathbf{w}}_i^{A_i} - \dot{\mathbf{c}}_i, \tag{73}$$

since $\mathbf{a}_i$ and $\mathbf{u}_i^{A_i}$ are time-invarient. In Eq. (73), the direction vector of $\dot{\mathbf{w}}_i^{A_i}$ is parallel to $\hat{\mathbf{l}}_i^{A_i}$ since $\dot{\mathbf{w}}_i \perp \mathbf{w}_i$. Thus, $\dot{\mathbf{w}}_i^{A_i}$ can be represented as follows:

$$\dot{\mathbf{w}}_i^{A_i} = -r_i\dot{\theta}_i\hat{\mathbf{l}}_i^{A_i}, \tag{74}$$

and

$$\frac{d}{dt}\mathbf{R}_i = \mathbf{R}_i^*\dot{\mathbf{R}}_{z_i} = \dot{\gamma}_i\left[\mathbf{R}_i^*\hat{\mathbf{k}}\right]_\times \mathbf{R_i} \tag{75}$$

since $\dot{\mathbf{R}}_i^* = 0$. As a consequence, Eq. (73) can be rewitten as

$$\dot{\mathbf{l}}_i = \dot{\gamma}_i\left[\mathbf{R}_i^*\hat{\mathbf{k}}\right]_\times(\mathbf{u}_i + \mathbf{w}_i) - r_i\dot{\theta}_i\hat{\mathbf{l}}_i - \dot{\mathbf{c}}_i. \tag{76}$$

By substituting Eq. (76) in Eq. (71), the relation between the rate of change of the length of cable i and the generalized velocity is obtained by

$$\dot{\ell}_i + r_i\dot{\theta}_i = -\hat{\mathbf{l}}_i^T\dot{\mathbf{p}} - (\mathbf{r}_i \times \hat{\mathbf{l}}_i)^T\boldsymbol{\omega}, \tag{77}$$

where note that the vector of the first term of the right side in Eq. (76) and $\hat{\mathbf{l}}_i$ are always orthogonal, thus their dot product is zero. Finally, by expanding Eq. (77) with all cables, Eq. (12) can be obtained.

REFERENCES

[1] J. Fink, N. Michael, S. Kim, and V. Kumar, "Planning and control for cooperative manipulation and transportation with aerial robots," *Int. J. Robot. Res.*, vol. 30, no. 3, pp. 324–334, Mar. 2011.
[2] L. Barbazza, D. Zanotto, G. Rosati, and S. K. Agrawal, "Design and optimal control of an underactuated cable-driven micro–macro robot," *IEEE Robot. Autom. Lett.*, vol. 2, no. 2, pp. 896–903, Apr. 2017.
[3] L. Scalera, A. Gasparetto, and D. Zanotto, "Design and experimental validation of a 3-DOF underactuated pendulum-like robot," *IEEE/ASME Trans. Mechatronics*, vol. 25, no. 1, pp. 217–228, Feb. 2020.
[4] G. Previati, M. Gobbi, and G. Mastinu, "Measurement of the mass properties of rigid bodies by means of multi-filar pendulums—Influence of test rig flexibility," *Mech. Syst. Signal Process.*, vol. 121, pp. 31–43, Apr. 2019.
[5] M. Gobbi, G. Mastinu, and G. Previati, "A method for measuring the inertia properties of rigid bodies," *Mech. Syst. Signal Process.*, vol. 25, no. 1, pp. 305–318, Jan. 2011.
[6] D. Surdilovic, J. Zhang, and R. Bernhardt, "STRING-MAN: Wire-robot technology for safe, flexible and human-friendly gait rehabilitation," in *Proc. IEEE 10th Int. Conf. Rehabil. Robot.*, Jun. 2007, pp. 446–453.
[7] G. Rosati, P. Gallina, and S. Masiero, "Design, implementation and clinical tests of a wire-based robot for neurorehabilitation," *IEEE Trans. Neural Syst. Rehabil. Eng.*, vol. 15, no. 4, pp. 560–569, Dec. 2007.
[8] I. B. Hamida, M. A. Laribi, A. Mlika, L. Romdhane, S. Zeghloul, and G. Carbone, "Multi-objective optimal design of a cable driven parallel robot for rehabilitation tasks," *Mechanism Mach. Theory*, vol. 156, Feb. 2021, Art. no. 104141.
[9] J.-P. Merlet and D. Daney, "A portable, modular parallel wire crane for rescue operations," in *Proc. IEEE Int. Conf. Robot. Autom.*, May 2010, pp. 2834–2839.
[10] M. Carricato and J.-P. Merlet, "Stability analysis of underconstrained cable-driven parallel robots," *IEEE Trans. Robot.*, vol. 29, no. 1, pp. 288–296, Feb. 2013.
[11] M. Carricato, "Direct geometrico-static problem of underconstrained cable-driven parallel robots with three cables," *J. Mech. Robot.*, vol. 5, no. 3, Aug. 2013, Art. no. 031008.
[12] G. Abbasnejad and M. Carricato, "Direct geometrico-static problem of underconstrained cable-driven parallel robots with n cables," *IEEE Trans. Robot.*, vol. 31, no. 2, pp. 468–478, Apr. 2015.
[13] G. Abbasnejad and M. Carricato, "Direct geometrico-static problem of underconstrained cable-driven parallel robots with five cables," in *Computational Kinematics*. Cham, Switzerland: Springer, 2014, pp. 59–66.
[14] A. Berti, J.-P. Merlet, and M. Carricato, "Solving the direct geometrico-static problem of underconstrained cable-driven parallel robots by interval analysis," *Int. J. Robot. Res.*, vol. 35, no. 6, pp. 723–739, 2016.
[15] U. A. Mishra and S. Caro, "Forward kinematics for suspended under-actuated cable-driven parallel robots with elastic cables: A neural network approach," *J. Mech. Robot.*, vol. 14, no. 4, pp. 1–11, Aug. 2022.
[16] U. A. Mishra and S. Caro, "Forward kinematics for suspended under-actuated cable-driven parallel robots: A neural network approach," in *Proc. 45th Mech. Robot. Conf. (MR)*, vol. 8B, Aug. 2021, Art. no. V08BT08A053.
[17] M. Carricato, "Inverse geometrico-static problem of underconstrained cable-driven parallel robots with three cables," *J. Mech. Robot.*, vol. 5, no. 3, 2013, Art. no. 031002.

[18] M. Carricato, G. Abbasnejad, and D. Walter, "Inverse geometrico-static analysis of under-constrained cable-driven parallel robots with four cables," in *Latest Advances in Robot Kinematics*. Cham, Switzerland: Springer, 2012, pp. 365–372.
[19] N. Yanai, M. Yamamoto, and A. Mohri, "Inverse dynamics analysis and trajectory generation of incompletely restrained wire-suspended mechanisms," in *Proc. IEEE Int. Conf. Robot. Autom. (ICRA)*, May 2001, pp. 3489–3494.
[20] M. Yamamoto, N. Yanai, and A. Mohri, "Trajectory control of incompletely restrained parallel-wire-suspended mechanism based on inverse dynamics," *IEEE Trans. Robot.*, vol. 20, no. 5, pp. 840–850, Oct. 2004.
[21] T. Heyden and C. Woernle, "Dynamics and flatness-based control of a kinematically undetermined cable suspension manipulator," *Multibody Syst. Dyn.*, vol. 16, no. 2, pp. 155–177, 2006.
[22] C. Gosselin, P. Ren, and S. Foucault, "Dynamic trajectory planning of a two-DOF cable-suspended parallel robot," in *Proc. IEEE Int. Conf. Robot. Autom.*, May 2012, pp. 1476–1481.
[23] N. Zoso and C. Gosselin, "Point-to-point motion planning of a parallel 3-DOF underactuated cable-suspended robot," in *Proc. IEEE Int. Conf. Robot. Autom.*, May 2012, pp. 2325–2330.
[24] C. Gosselin, "Global planning of dynamically feasible trajectories for three-DOF spatial cable-suspended parallel robots," in *Cable-Driven Parallel Robots*. Cham, Switzerland: Springer, 2013, pp. 3–22.
[25] C. Gosselin and S. Foucault, "Dynamic point-to-point trajectory planning of a two-DOF cable-suspended parallel robot," *IEEE Trans. Robot.*, vol. 30, no. 3, pp. 728–736, Jun. 2014.
[26] X. Jiang and C. Gosselin, "Dynamic point-to-point trajectory planning of a three-DOF cable-suspended parallel robot," *IEEE Trans. Robot.*, vol. 32, no. 6, pp. 1550–1557, Dec. 2016.
[27] X. Jiang, E. Barnett, and C. Gosselin, "Dynamic point-to-point trajectory planning beyond the static workspace for six-DOF cable-suspended parallel robots," *IEEE Trans. Robot.*, vol. 34, no. 3, pp. 781–793, Jun. 2018.
[28] P. Dion-Gauvin and C. Gosselin, "Dynamic point-to-point trajectory planning of a three-DOF cable-suspended mechanism using the hypocycloid curve," *IEEE/ASME Trans. Mechatronics*, vol. 23, no. 4, pp. 1964–1972, Aug. 2018.
[29] N. Zhang and W. Shang, "Dynamic trajectory planning of a 3-DOF under-constrained cable-driven parallel robot," *Mechanism Mach. Theory*, vol. 98, pp. 21–35, Apr. 2016.
[30] E. Ida, T. Bruckmann, and M. Carricato, "Rest-to-rest trajectory planning for underactuated cable-driven parallel robots," *IEEE Trans. Robot.*, vol. 35, no. 6, pp. 1338–1351, Dec. 2019.
[31] L. Ramli, Z. Mohamed, and H. I. Jaafar, "A neural network-based input shaping for swing suppression of an overhead crane under payload hoisting and mass variations," *Mech. Syst. Signal Process.*, vol. 107, pp. 484–501, Jul. 2018.
[32] E. Idá, S. Briot, and M. Carricato, "Robust trajectory planning of underactuated cable-driven parallel robot with 3 cables," in *Proc. Int. Symp. Adv. Robot Kinematics*. Cham, Switzerland: Springer, 2020, pp. 65–72.
[33] J. Park, O. Kwon, and J. H. Park, "Anti-sway trajectory generation of incompletely restrained wire-suspended system," *J. Mech. Sci. Technol.*, vol. 27, no. 10, pp. 3171–3176, Oct. 2013.
[34] S. W. Hwang, J.-H. Bak, J. Yoon, and J. H. Park, "Oscillation reduction and frequency analysis of under-constrained cable-driven parallel robot with three cables," *Robotica*, vol. 38, no. 3, pp. 375–395, Mar. 2020.
[35] E. Ida, S. Briot, and M. Carricato, "Natural oscillations of underactuated cable-driven parallel robots," *IEEE Access*, vol. 9, pp. 71660–71672, 2021.
[36] S. W. Hwang, J.-H. Bak, J. Yoon, J. H. Park, and J.-O. Park, "Trajectory generation to suppress oscillations in under-constrained cable-driven parallel robots," *J. Mech. Sci. Technol.*, vol. 30, no. 12, pp. 5689–5697, Dec. 2016.
[37] L. Y. Pao, "Multi-input shaping design for vibration reduction," *Automatica*, vol. 35, no. 1, pp. 81–89, Jan. 1999.
[38] T. Singh and W. Singhose, "Input shaping/time delay control of maneuvering flexible structures," in *Proc. Amer. Control Conf.*, May 2002, pp. 1717–1731.

SUNG WOOK HWANG received the B.S. degree in mechanical automotive engineering from Pukyong National University, South Korea, in 2012, and the M.S. degree in mechanical engineering from Hanyang University, in 2014. He is currently pursuing the Ph.D. degree. His research interests include robot dynamics and control, humanoid robots, legged robots, and cable-driven parallel robots.

DEOK HA KIM received the B.S. degree in mechanical engineering from Hanyang University, Seoul, South Korea, in 2014, where he is currently pursuing the Ph.D. degree with the Department of Mechanical Engineering. His research interests include cable-driven robots, legged robots, robot dynamics, and optimal control.

JAEHWAN PARK received the B.S. and M.S. degrees in mechanical engineering from Hanyang University, Seoul, South Korea, in 2010 and 2012, respectively, where he is currently pursuing the Ph.D. degree with the School of Mechanical Engineering. He was a Researcher at the Korea Institute of Industrial Technology (KITECH), Ansan, South Korea, from 2012 to 2015. Since 2015, he has been working with the Korea Institute of Science and Technology (KIST), as a Student Researcher. His research interests include legged robots, cable-driven robots, and wearable robots.

JONG HYEON PARK (Member, IEEE) received the B.S. degree in mechanical engineering from Seoul National University, Seoul, South Korea, in 1981, and the S.M. and Ph.D. degrees from the Massachusetts Institute of Technology (MIT), Cambridge, MA, USA, in 1983 and 1991, respectively. Since 1992, he has been with the School of Mechanical Engineering, Hanyang University, Seoul, where he is currently a Professor. He was a Korea Science and Engineering Foundation Japan Society for the Promotion of Science Visiting Researcher at Waseda University, Tokyo, Japan, in 1999; a KOSEF-CNR Visiting Researcher at the Scuola Superiore Sant'Anna, Pisa, Italy, in 2000; a Visiting Scholar at MIT, from 2002 to 2003; a Visiting Scholar at Purdue University, West Lafayette, IN, USA, from 2008 to 2010; and a Visiting Scholar at the University of Stuttgart, Germany, from 2019 to 2020. He was also Associated with Brooks Automation Inc., Chelmsford, MA, USA, from 1991 to 1992 and from 2001 to 2002. His research interests include biped robots, robot dynamics and control, haptics, and biorobots. He is a member of The Korean Society of Mechanical Engineers, The Korean Society of Automotive Engineers, Korean Society of Precision Engineering, and *Journal of Institute of Control, Robotics and Systems*. For six years, he has served as a Senior Editor of the *Journal of Mechanical Science and Technology*.